scientific reports

Check for updates

OPEN

Synthesis and catalytic activity of silver- reduced graphene oxide and silver- magnetite- reduced graphene oxide nanocomposites in the reduction of 4-nitrophenol

Bahareh Kabiri & Hannaneh Heidari✉

The catalytic reduction of 4-nitrophenol (4-NP) to 4-aminophenol (4-AP) is vital for environmental remediation. This study synthesizes and assesses silver-reduced graphene oxide (Ag/rGO) and silver-magnetite-reduced graphene oxide (Ag/Fe_2O_4/rGO) nanocomposites for 4-NP reduction. Various reducing agents—ascorbic acid (AA), hydrazine hydrate (HH), sodium borohydride (SBH), and cellulose nanofibers (NFC)—were employed under reflux (R), hydrothermal (H), and ultrasonic (U) conditions. Drying methods (oven-drying (O) and freeze-drying (F)) and CTAB as a stabilizer were explored to optimize Ag NP distribution. The nanocomposites were characterized using FT-IR, XRD, FE-SEM, EDS, TEM, BET, TGA, ICP-OES, and VSM. XRD confirmed Ag NP formation with crystallite sizes of 12–23 nm. FE-SEM and TEM showed uniform distribution of cubic Fe_2O_4 and spherical Ag NPs (approximately 50 nm) on GO. The Ag/Fe_2O_4/rGO(O)-AA-U-F nanocomposite demonstrated the highest catalytic activity, with a pseudo-first-order rate constant (k) of 1.81 min^{-1} and a specific activity parameter (k') of 180.77 $min^{-1}.g^{-1}$. This nanocomposite exhibited a mesoporous structure with a high specific surface area (226.9 m^2/g) and uniform Ag and Fe_2O_4 nanoparticle distribution on rGO. The combination of ascorbic acid (AA) and freeze-drying (F) yielded nanocomposites with superior catalytic performance due to their porous structure and uniform nanoparticle dispersion.

Keywords Ag/Fe_3O_4/rGO nanocomposite, Catalytic reduction, 4-NP

Water pollution caused by organic compounds released from the textile, printing, and pharmaceutical industries presents a significant environmental challenge. Many organic pollutants are nonbiodegradable and highly toxic, posing risks to human and animal health. Exposure to these substances can lead to mutations and cancer[1]. Consequently, significant effort has been made to remove these pollutants using various methods. 4-NP is one of the main water pollutants used in the production of certain pharmaceuticals such as acetaminophen, fungicides, methyl and ethyl parathion insecticides, and dyes for leather darkening. The reduction of 4-NP using excess sodium borohydride in the presence of microgels functionalized with metal nanoparticles is commonly used to assess the catalytic activity of various systems. This reduction process converts 4-NP to 4-AP, which is a crucial commercial intermediate used in the production of analgesics and antipyretics. In addition, 4-NP is among the most persistent pollutants found in industrial wastewater[2]. The development of efficient and environmentally friendly catalysts for this reaction has gained attention and remains a challenge. Using aerogel nanocomposites as a catalyst is a suitable option for accelerating this reaction. An aerogel recognizes a porous solid as a type of dried gel with a very high relative pore volume and extremely low weight. They can be fabricated with various shapes and sizes. In 1931, Steven Kistler was the first to produce these materials in an autoclave[3].

Reduced graphene oxide (rGO) is a form of graphene whose oxygen content is reduced through physical methods, such as heating, chemical reduction, and hybrid reduction, which combine both physical and chemical methods. rGO possesses properties similar to those of pure graphene, including mechanical, optical, and conductive capabilities, owing to its heterogeneous structure, consisting of a graphene base layer with structural defects. The structural properties of reduced graphene oxide enable a variety of applications, such as sensing, biological, environmental, and catalytic applications, as well as in electronic devices and energy storage.

Department of Inorganic Chemistry, Faculty of Chemistry, Alzahra University, Tehran, Iran. ✉email: h.heidari@alzahra.ac.ir

Graphene-based aerogels (GAs) are three-dimensional scaffolding materials that are lighter than air. Owing to their remarkable properties, including mechanical strength, high thermal resistance, electrical conductivity, and absorption capacity, they have gained significant attention in recent years[4]. Conventional methods used in the synthesis of GO aerogels include hydrothermal reduction, chemical reduction, crosslinking methods, and template-based reduction[5]. The chemical reduction of compounds is considered significant in chemistry, utilizing various reducing agents. These reducing agents include hydrazine hydrate, ascorbic acid, sodium borohydride, various nanocellulose, sugars such as glucose, alkaline solutions of Fe powder, hydroquinone, hexamethylenetetramine, hydroiodic acid, sodium, and potassium, which can be used in liquid or vapor environments at moderate or even room temperatures[6]. This method does not require chemical linkers, high temperatures, or high pressures compared to hydrothermal methods. The chemical reduction of graphene-based materials often results in a decreased surface area, as the graphene layers tend to restack owing to π–π interactions[7].

Nanocatalysts are among the most important research areas in nanotechnology, facilitating many significant reactions such as the reduction of pollutants (e.g., 4-NP), oxidation of carbon monoxide, decomposition of toxic gases (e.g., nitrogen dioxide), and methanol oxidation. Many properties of materials change when they are at the nanoscale, but three critical factors contributing to the catalytic properties of nanomaterials are their very small size, high surface-to-volume ratio, and increased number of surface atoms. When the particles become nanoscale, the number of surface atoms increases, making them highly active and prone to chemical reactions[8]. Noble metal catalysts including Au, Pt, Ag, and Ni are commonly used because of their high catalytic activity and favorable selectivity[9,10]. Because nanoparticles tend to aggregate into larger particles, which leads to a decrease in their activity, an effective method to inhibit the agglomeration of nanoparticles is to immobilize them on various substrates, including graphene oxide[10,11], MOF[12], cellulose[13], zeolite[14], mxene[15] Justicia tranquebariensis (JT) extract[16], polyaniline[17], TiO_2[18], CeO_2[19,20], spinel[21], and so on[22].

The synthesis of Ag NPs on rGO and Fe_3O_4/rGO nanocomposites involves the reduction of silver ions (Ag^+) to metallic silver (Ag^0). The choice of reducing agent plays a critical role in determining the size, distribution, and catalytic activity of the resulting Ag NPs. In this study, four different reducing agents were used: ascorbic acid, hydrazine hydrate, sodium borohydride, and cellulose nanofibers. Ascorbic acid was selected for its environmentally friendly nature and ability to provide controlled reduction, leading to well-dispersed Ag NPs with uniform size distribution[23]. Hydrazine hydrate, a strong reducing agent, was used to achieve rapid and complete reduction of Ag^+ ions[24], while sodium borohydride was employed for its ability to produce small Ag NPs with high surface area[25]. Cellulose nanofibers, a green and sustainable reducing agent, were chosen for their dual role as both reducing and stabilizing agents, preventing NP aggregation and promoting uniform distribution[26]. The choice of reducing agent significantly impacts the catalytic performance of the nanocomposites. Smaller and well-dispersed Ag NPs, achieved through the use of appropriate reducing agents, exhibit higher catalytic activity due to their increased surface area and accessibility of active sites[18,22]. Additionally, the use of environmentally friendly reducing agents aligns with the principles of green chemistry and sustainable synthesis[27].

This study aims to investigate and compare the catalytic activity of Ag nanocomposites on reduced graphene oxide (rGO) substrates using various reducing agents, employing diverse methods in both powdered and aerogel forms, as well as in magnetite (Ag/Fe_3O_4/rGO) and non-magnetite (Ag/rGO) configurations, in the catalytic reduction of 4-NP in the presence of excess $NaBH_4$.

Materials and methods

Natural graphite flakes (99% carbon basis, 50 mesh particle size), potassium permanganate ($KMnO_4$, ≥ 99%), iron(III) chloride hexahydrate ($FeCl_3.6H_2O$, ≥ 99%), iron(II) sulfate heptahydrate ($FeSO_4.7H2O$, ≥ 99%), sodium hydroxide (NaOH, ≥ 98%), hydrochloric acid (HCl, 37%), sulfuric acid (H_2SO_4, 98%), phosphoric acid (H_3PO_4 99%), hydrogen peroxide (H_2O_2, 30%), ethanol (C_2H_5OH, 99%), ascorbic acid, hydrazine hydrate 98%, nano fiber cellulose (mechanical product 3.3 wt%– Nano Novin Polymer Company, Iran), cetyltrimethylammonium bromide (CTAB), silver nitrate ($AgNO_3$, ≥ 99%), sodium borohydride ($NaBH_4$, ≥ 98%), and 4-NP ($O_2NC_6H_4OH$, ≥ 99%) were purchased from Merck Company.

UV–Vis measurements were performed using Lambda-25 UV–vis spectrometer (Perkin-Elmer, Waltham, Massachusetts, USA). IR spectra were recorded from KBr disk using FT-IR Bruker Tensor 27 instrument. The morphology of samples was analyzed with a TESCAN MIRA3 FE-SEM. TEM images were taken using a Zeiss instrument, model EM900. X-ray diffraction data were collected using a PANalytical X'Pert Pro diffractometer with Cu-Kα radiation at 40 kV and 30 mA, scanning a 2θ range of 0–80 degrees. Thermogravimetric measurements were performed using the STA 1500 instrument.

Preparation of graphene oxide

The synthesis of GO was conducted using a modified Hummers' method[28]. Initially, 30 mL of H_2SO_4 and 3.3 mL of H_3PO_4 were added to a beaker and cooled in an ice bath. After 30 min, 1 g of graphite and 6 g of $KMnO_4$ were added, and the mixture was stirred for another 30 min until homogeneous. The system was then allowed to react at 35 °C for 2 h. Following this, 100 mL of deionized water was introduced, and 10 mL of H_2O_2 was added, continuing the reaction at 35 °C for 24 h. The resulting yellow solution was washed with 10% HCl and deionized water. Finally, one portion of the obtained graphene oxide was dried in an oven at 60 °C for 24 h (GO (O)), while the other portion was freeze-dried at − 60 °C and 0.05 atm for 24 h (GO (F)).

Preparation of Ag/rGO nanocomposites by reflux method

GO powder synthesized was dispersed in distilled water at a concentration of 5 mg/mL. Subsequently, 20 mL of $AgNO_3$ solution containing ammonia at a concentration of 10 mg/mL was added to 40 mL of the prepared GO

solution. The resulting mixture was sonicated for 10 min. Following this, 1.0 g of ascorbic acid was incrementally added, and the reaction mixture was stirred at a temperature of 90 °C for a duration of 2.5 h.

The product was dried in two methods; the powder form was obtained by oven-drying at 60 °C for 24 h (Ag/rGO (O)-AA-R-O) and the aerogel form as obtained by freeze-drying at − 60 °C and 0.05 atm for 24 h (Ag/rGO (O)-AA-R-F). For comparison, the Ag/rGO composite was synthesized by reflux with different reducing agents such as hydrazine hydrate, sodium borohydride and cellulose nanofibers (Ag/rGO (O)-HH-R-O), (Ag/rGO (O)-SBH-R-O), (Ag/rGO (O)-NFC-R-O) and oven-dried, respectively. And freeze-dried (Ag/rGO (O) -NFC-R-F).

Preparation of Ag/rGO nanocomposites by hydrothermal method

0.132 g of oven-dried graphene oxide are dispersed in 26.5 mL of distilled water using ultrasonic waves for one hour. Then, 0.132 g of $AgNO_3$ are dissolved in 13.2 mL of ammonia solution and added to the graphene oxide. After ultrasonic treatment for 10 min, 0.66 g of ascorbic acid are introduced as a reducing agent. The mixture is placed in an autoclave at 95 °C for 2.5 h, after which it is washed with a 1:5 ethanol–water mixture and oven-dried at 60 °C (Ag/rGO (O)-AA-H-O).

Preparation of Ag/rGO with CTAB

0.1 g GO powder obtained from modified Hummer's method was dispersed in 20 mL distilled water. 10 mL of CTAB solution (10 mg/mL) was added to GO solution. Subsequently, 10 mL $AgNO_3/NH_3$ (10 mg/mL) was added to solution. The mixture was then sonicated for 10 min. Subsequently, 0.5 g of L-hydrazine hydrate was added gradually, and the reaction mixture was stirred at a temperature of 90 ± 5 °C for a duration of 2.5 h. The Half of product was freeze-dried at -60 °C and 0.05 atm for 24 h (Ag/rGO (O)-HH-R-F- CTAB) and the remaining portion was oven-dried at 60 °C (Ag/rGO (O)-HH-R-O- CTAB).

Preparation of Ag/Fe_3O_4/rGO nanocomposites

In the first step, the GO solution with a concentration of 1 mg/mL was prepared by dispersing 0.05 g GO into 50 mL of distilled water using ultrasonic agitation for 30 min. Subsequently, 0.2332 g $FeCl_3.6H_2O$ and 0.1119 g $FeSO_4.7H_2O$ were introduced into the GO solution, and the mixture was stirred at 60 °C for 30 min. Subsequently, a solution of 2 M NaOH was added to adjust the pH to 10. After vigorous stirring for an additional 30 min, the Fe_3O_4/GO composite was magnetically separated, washed with distilled water until neutral, and dried at 60 °C. For comparison, pure Fe_3O_4 nanoparticles were synthesized using the same procedure, excluding the addition of GO.

A measured amount of 0.05 g of the synthesized Fe_3O_4/GO composite was then dispersed in 50 mL of distilled water through ultrasonic treatment for 30 min to obtain a clear solution at a concentration of 1 mg/mL. In the next step, 25 mL of 0.1 M NaOH and 25 mL of 5 mM $AgNO_3$ were sequentially added to the 50 mL Fe_3O_4/GO solution at room temperature while stirring. Following this, 50 mL of a 2 g/L ascorbic acid solution was introduced into the mixture, and ultrasonic irradiation was applied for an additional 30 min. The resulting composite was then collected using a magnet and washed with anhydrous ethanol to remove any unreacted materials.

The product was dried in two ways; the powder form was obtained by oven-drying at 60 °C for 24 h (Ag/Fe_3O_4/rGO(O)-AA-U-O) and the aerogel form as obtained by freeze drying at − 60 °C and 0.05 atm for 24 h with oven dried GO (Ag/Fe_3O_4/rGO(O)-AA-U-F) or freeze-dried GO (Ag/Fe_3O_4/rGO(F)-AA-U-O, and Ag/Fe_3O_4/rGO(F)-AA-U-F). For comparison, the Ag/Fe_3O_4/rGO composite was synthesized with nanofiber cellulose (Ag/Fe_3O_4/rGO (O) -NFC-U-O, Ag/Fe_3O_4/rGO(O)-NFC-U-F).

Catalytic reduction of 4-NP

The catalytic reduction was conducted using a mixture of 0.25 mL of 20 mM 4-NP, 0.25 mL of 0.1 M sodium borohydride, and 19.5 mL of deionized water, with 10 mg of each catalyst. As the reaction progressed, the initial yellow color faded to colorless. Aliquots were taken at regular intervals, and UV–vis absorption spectra were recorded until the absorption peak of 4-NP disappeared completely.

Results and discussion

Catalyst characterization

FTIR spectra of pure GO and Ag/rGO composites are illustrated in Fig. 1a. The FTIR spectrum of GO displayed characteristic peaks at 1052 cm^{-1} (OH), 1218 cm^{-1} (C–O–C), 1400 cm^{-1} (C–OH), 1627 cm^{-1} (C=C), 1736 cm^{-1} (C=O in carboxylic acid and carbonyl groups), and 3423 cm^{-1} (–OH). In contrast, the spectrum for the rGO, revealed a notable decrease in the peak intensity at 3423 cm^{-1}, 1736 cm^{-1}, and 1218 cm^{-1} corresponding to OH, C=O, and C–O–C, respectively. This observation suggests the reduction of graphene oxide has been successfully carried out using all employed reducing agents. The diminished intensity of these groups confirmed their active role in the reduction process. Their participation facilitated the conversion of Ag ions into nanoparticles[16]. Additionally, in Fig. 1b, the band at 582 cm^{-1} was attributed to the Fe–O vibrational mode of Fe_3O_4 in Ag/rGO/Fe_3O_4 composite. In Fig. 1c the bands at 2837 cm^{-1} and 2918 cm^{-1} that were attributed to C-H band, show more intensive than peaks in Fig. 1a as the presence of CTAB[29]. This similarity arises from the presence of common functional groups, such as hydroxyl and carbonyl groups, in the structure of graphene oxide (GO), as well as the formation of metallic nanoparticles (Ag) and metal oxides (Fe_3O_4) in the composite samples. The hydroxyl and carbonyl groups act as active sites for the adsorption and activation of reactant molecules, while the metallic nanoparticles and metal oxides play a crucial role in electron transfer and enhancing catalytic activity. Thus, the similarity in the FT-IR peaks is not only expected but also indicative of the presence of essential structures and functional groups that contribute to the catalytic performance of the samples.

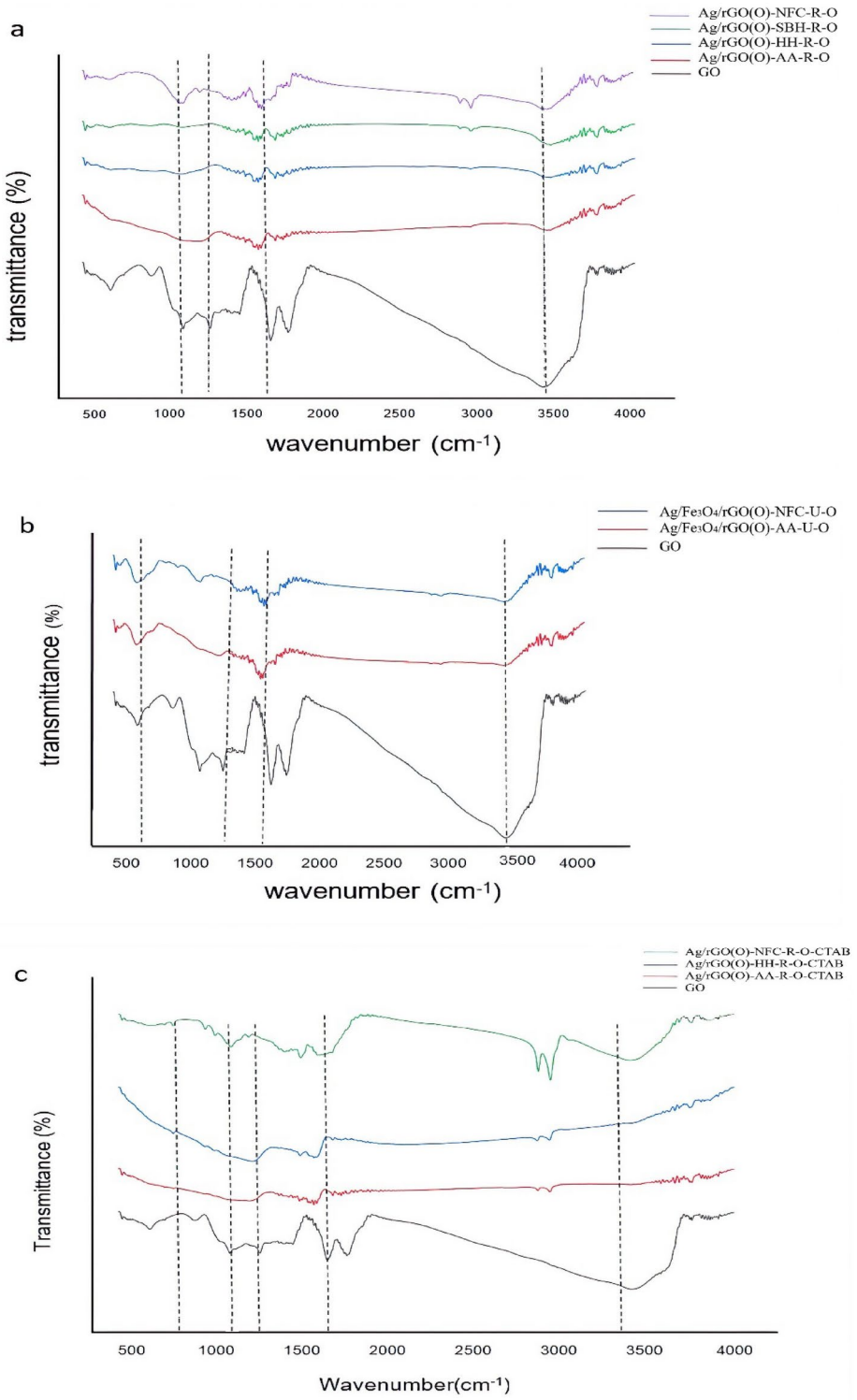

Fig. 1. FT-IR spectra of (**a**) Ag/rGO nanocomposites synthesized by different reductant and methods, (**b**) Ag/Fe_3O_4/rGO synthesized by different reductants, (**c**) Ag/rGO nanocomposites synthesized by different reductants and using CTAB.

XRD patterns of Ag/rGO composites are presented in Fig. 2. The X-ray diffractograms of the Ag/rGO composite peak at 38.22° is attributed to the significant growth of Ag NPs along the (111) crystallographic plane. Additional characteristic peaks at 44.31°, 64.56°, and 77.46° were indexed to the (200), (220), and (311) crystal planes, respectively, based on the face-centered cubic (fcc) structure of metallic Ag (JCPDS No. 04-0783)[20] (Fig. 2a). The presence of sharply defined and intense peaks indicates the successful chemical reduction of Ag

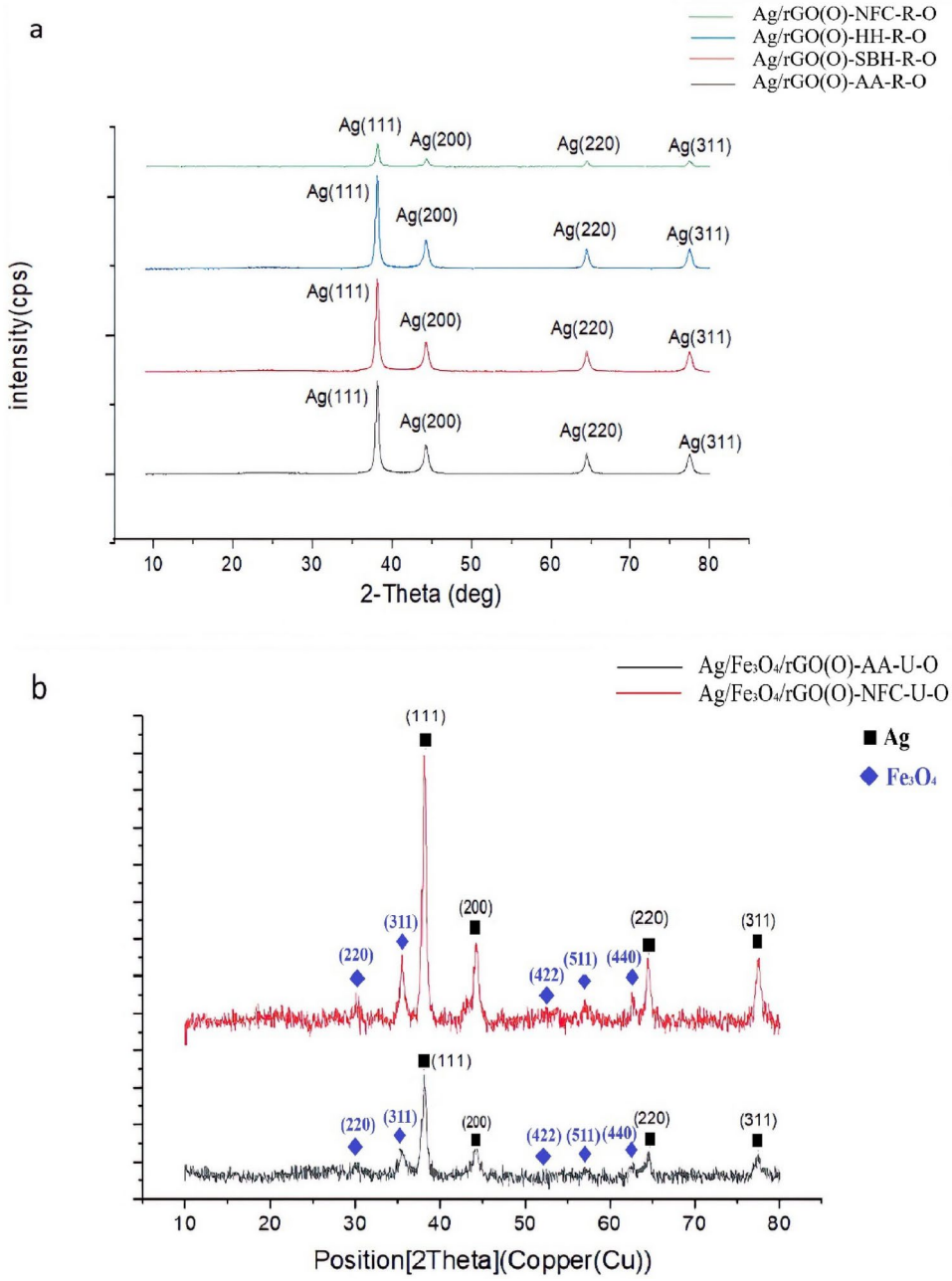

Fig. 2. XRD pattern of (**a**) Ag/rGO nanocomposites synthesized by different reductants, (**b**) Ag/Fe_3O_4/rGO synthesized by different redutants.

ions with the usage of ascorbic acid, hydrazine hydrate, sodium borohydride, and cellulose nanofibers leads to formation of high concentration of metallic Ag nanoparticles. Furthermore, the iron oxide phase in Fe_3O_4 NPs can be corroborated by the diffraction peaks observed at 30.2°, 35.4°, 43.5°, 53.7°, 57.1°, and 62.7°, which correspond to the (220), (311), (400), (422), (511), and (440) planes of the cubic spinel structure (JCPDS no. 87-2334)[17] (Fig. 2b).

The XRD pattern of the rGO typically shows a broad peak around 24–26°, corresponding to the (002) plane of graphitic carbon. The broad nature of this peak indicates the presence of disordered carbon structures in rGO[30].

The crystallite size of Ag NPs in the composites was calculated via XRD analysis using the Debye–Scherrer Eq. (1) (12–19 nm) and the Williamson-Hall Eq. (2) (13–23 nm). In the Debye–Scherrer Eq. (1), β is full width at half maximum of the most intense peak, λ is the X-ray wavelength ($\lambda_{Cu} = 1.54$ A °), θ is diffraction angle (Bragg's angle-the pick position), K is the shape factor (0.94) and τ is crystallite size. In the Williamson-Hall Eq. (2), ε is lattice strain and other parameters are like Eq. (1). The value of ε and the crystallite size can be determined by plotting a graph of $\beta\cos\theta$ versus $\sin\theta$. The slope of the graph represents the value of ε, while the intercept can indicate the crystallite size[20,31,32].

$$\tau = \frac{K \times \lambda}{\beta \cos\theta} \tag{1}$$

$$\beta \cos\theta = 4\varepsilon \sin\theta + \frac{K \times \lambda}{\tau} \tag{2}$$

The crystallite size calculated using the Scherrer equation often deviates from that determined by the Williamson-Hall method, suggesting the presence of significant lattice strain in the sample. While the Scherrer equation attributes peak broadening exclusively to crystallite size—resulting in an underestimated value—the Williamson-Hall method provides a more accurate evaluation by decoupling the effects of crystallite size and lattice strain, thereby yielding a more reliable estimate of crystallite dimensions.

The morphology of the Ag/rGO(O)-AA-R-O (Fig. 3a, b), Ag/rGO(O)-AA-R-F (Fig. 3c, d), Ag/rGO(O)-HH-R-F-CTAB (Fig. 3e, f), Ag/Fe_3O_4/rGO(O)-AA-U-O (Fig. 4a, b), and Ag/Fe_3O_4/rGO(O)-AA-U-F (Fig. 4c, d) was investigated by FE-SEM. As observed, a significant number of NPs were distributed on the surface of GO, indicating the in-situ formation of Ag nanoparticles. The use of CTAB as a stabilizer can optimize the distribution of Ag nanoparticles (Fig. 3e, f). EDS analysis was conducted to confirm the presence of C, O, and Ag elements in the composite. An increase in the prominent peak of Ag (25.86%) was noted, confirming the successful loading of Ag onto the surface of GO (Fig. 3g). Figure 4a, c (lower magnification) reveal a highly porous and rough surface structure, suggesting the presence of reduced graphene oxide (rGO) sheets decorated with nanoparticles. The layered structure seen in the micrograph (especially in c) is characteristic of rGO, which provides a high surface area for nanoparticle anchoring. Figure 4b, d (higher magnification) well-distributed Ag and Fe_3O_4 nanoparticles are visible in the range between 35 and 43 nm in diameter for Ag/Fe_3O_4/rGO(O)-AA-U-O and between 48 and 56 nm in diameter for Ag/Fe_3O_4/rGO(O)-AA-U-F. The uniform distribution of nanoparticles without excessive agglomeration suggests strong interactions between Ag, Fe_3O_4, and rGO.

The elemental mapping of Ag/Fe_3O_4/rGO(O)-AA-U-F have been shown in Fig. 4e-j. Ag nanoparticles are well distributed, confirming the successful deposition of Ag on the composite, The presence of iron suggests Fe_3O_4 (magnetite) nanoparticles are homogeneously dispersed, Oxygen is mainly associated with Fe_3O_4 and any residual oxygen-containing functional groups in rGO. And Carbon is widespread, confirming the presence of the rGO framework. The EDS elemental analysis table shows the presence of C (34.61%) confirms the rGO matrix, while O (31.35%) and Fe (25.55%) indicate Fe_3O_4 formation. The presence of Ag (8.50 wt%) suggests successful incorporation of Ag nanoparticles.

The Ag content in the catalyst (Ag/Fe_3O_4/rGO (O)-AA-U-O), as determined by ICP-OES analysis, was found to be 8000 ppm.

The typical TEM images of Ag/Fe_3O_4/rGO(O)-AA-U-F nanocomposite distributions are shown in Fig. 5. The TEM images show that the Ag Nps are relatively spherical and well-distributed on the GO substrate. However, some degree of aggregations could also be observed. The Fe_3O_4 particles are visible as cube-shaped structures in the image. The particles have an approximate size of 50 nm.

The study investigated the impact of different drying methods on the textural properties of Ag/rGO(O)-AA-R-O, Ag/rGO(O)-AA-R-F, Ag/Fe_3O_4/rGO(O)-AA-U-F composites. Table 1 displays the specific surface area measured using the BET method and the average pore diameter obtained from desorption isotherms according to BJH analysis. The BET isotherm exhibited a very high sorption and a clear hysteresis in the desorption curve that clearly indicates the presence of mesopores in the composite (Fig. S1).

The Ag/Fe_3O_4/rGO(O)-AA-U-F sample demonstrates the best performance among the tested materials, characterized by its high specific surface area (226.9 m^2/g), optimal pore volume (0.43 cm^3/g), and favorable mean pore diameter (7.74 nm). These properties enhance access to active surface sites and significantly improve performance in catalytic application. The Ag/rGO(O)-AA-R-F sample, with a moderate specific surface area (39.91 m^2/g) and low pore volume (0.056 cm^3/g), shows improved performance compared to Ag/rGO(O)-AA-R-O, though it remains inferior to Ag/Fe_3O_4/rGO(O)-AA-U-F. In contrast, the Ag/rGO(O)-AA-R-O sample, with its low specific surface area (18.41 m^2/g) and relatively high pore volume (0.086 cm^3/g), exhibits the lowest performance. This analysis highlights that the incorporation of Fe_3O_4 nanoparticles and the optimization of the porous structure with freeze-dryer can significantly enhance the material's performance in catalytic and adsorption applications.

The magnetization curve depicted in Fig. 6 suggests that Ag/Fe_3O_4/rGO(O)-AA-U-O demonstrates superparamagnetic-like behavior at room temperature. The saturation magnetization (Ms) of the copmposite is ca 13.2 emu. g^{-1} at 14 kOe which is lower than the specific saturation magnetization of Fe_3O_4 (47emu.g^{-1}).

The thermal behavior of Ag/Fe_3O_4/rGO(O)-AA-U-O was evaluated using thermogravimetric analysis (TGA) at a heating rate of 10 °C min^{-1} under a nitrogen atmosphere (Fig. 7). The TGA curve reveals three weight loss steps. The first weight loss, about 2%, occurs at 100 °C and is mainly due to the evaporation of physically absorbed water. While the weight loss in the range of 100–300 °C corresponded to the decomposition of oxygen-containing functional groups on the rGO surface. The reduction of GO to rGO resulted in a decrease in the intensity of this step, indicating the successful removal of these functional groups. The weight loss in the range of 300–600 °C was associated with the combustion of the carbon skeleton of rGO. The remaining residue at high temperatures included both metallic Ag and Fe_3O_4, confirming the presence of these components in the nanocomposite. The TGA results demonstrate the high thermal stability and compositional integrity of the nanocomposites, making them suitable for applications that require thermal resistance, such as catalysis at elevated temperatures[25,33].

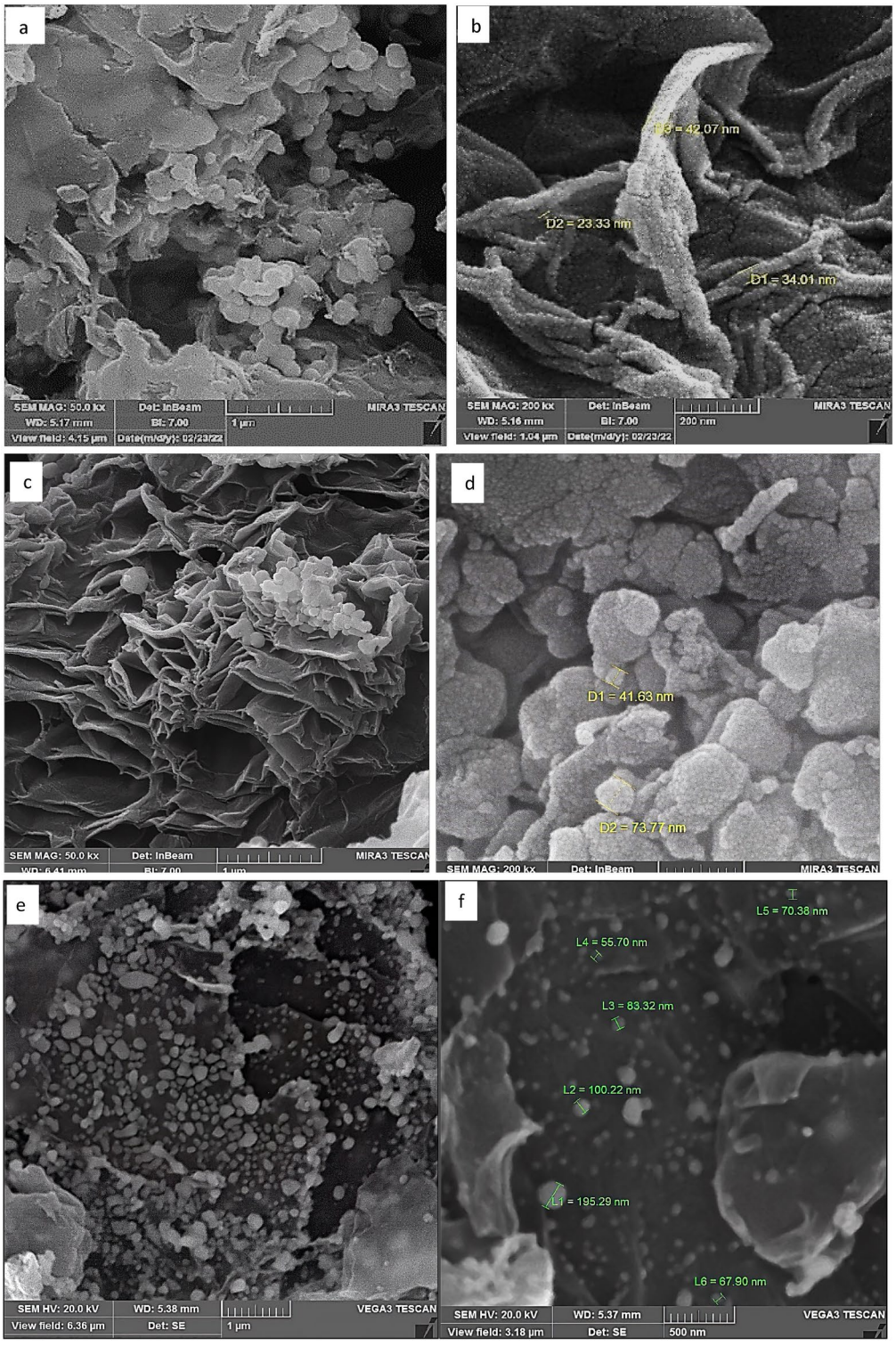

Fig. 3. FESEM micrographs of (**a**, **b**) Ag/rGO(O)-AA-R-O, (**c**, **d**) Ag/rGO(O)-AA-R-F. (**e**, **f**) Ag/rGO(O)-HH-R-F-CTAB. (**g**) EDS spectrum and elemental analysis results of Ag/rGO(O)-AA-R-F.

The evaluation of catalytic performance for 4-NP reduction

The UV spectrum of the catalytic reductionof 4-NP in the presence of excess $NaBH_4$ by Ag/rGO(O)-AA-R-O, Ag/rGO(O)-AA-R-F and Ag/rGO(O)-AA-H-O nanocomposite catalysts are shown in Fig. 8a–c respectively. In Fig. 8d, by comparing the plots of Ln (A_t/A_0) in terms of time at a wavelength of 400 nm for 3 catalysts made using ascorbic acid reductant, it can be concluded that in general, when the catalyst is synthesized by reflux method, the reduction reaction of 4-NP is performed faster than when the catalyst is synthesized by hydrothermal

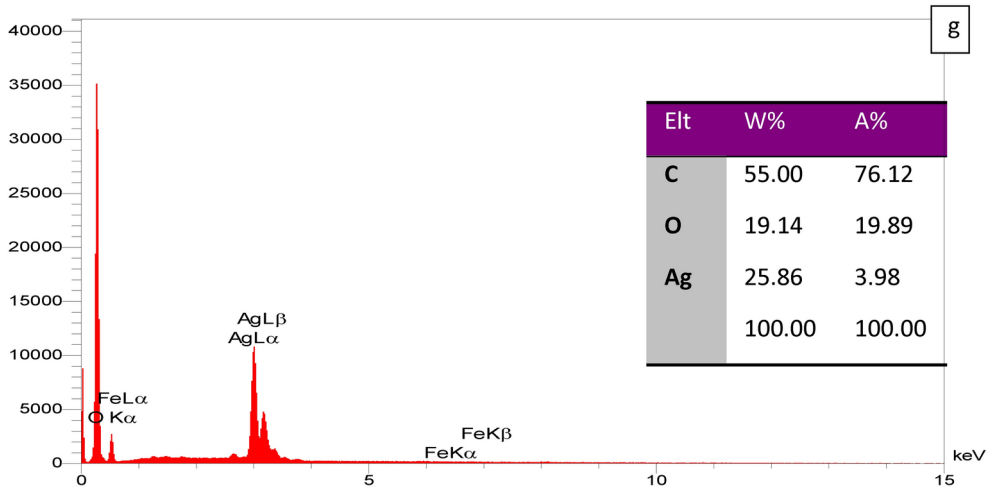

Figure 3. (continued)

method, which shows the difference in the structure of the two catalysts in the two types of synthesis methods. In addition to the synthesis method, differences in drying the catalyst, affect its performance and, as can be seen, when the catalyst dries in the freeze dryer, due to more porosity in the structure of the catalyst, than the catalyst dried in the oven shows better performance.

The UV spectrum of the catalytic reduction of 4-NP in the presence of excess $NaBH_4$ by Ag/rGO(O)-AA-R-O, Ag/rGO(O)-HH-R-O, Ag/rGO(O)-SBH-R-O, Ag/rGO(O)-NFC-R-O nanocomposite catalysts are shown in Fig. 9a–d respectively. In Fig. 9e, the effect of different reducers on the catalytic effect of synthesized Ag/rGO catalysts under the same conditions is investigated. As shown in the Fig. 9, the catalyst synthesized with nanofiber cellulose, hydrazine hydrate, and ascorbic acid reducing agents have the most effect on increasing the rate of catalytic reduction of 4-NP, respectively and sodium borohydride has the least effect. An experiment to evaluate the reduction of 4- NP was performed using precursors as a substrate for nanocomposites, lasting 50 min. The findings revealed that graphene oxide, reduced graphene oxide, and cellulose nanofibers, when used individually, had no effect on the dye reduction process over a duration of 50 min (Fig. S2).

The UV spectrum of the catalytic reduction of 4-NP in the presence of excess $NaBH_4$ by magnetic nanocomposite catalysts including Ag/Fe_3O_4/rGO(O)-AA-R-O, Ag/Fe_3O_4/rGO-AA-R-F, Ag/Fe_3O_4/rGO(F)-AA-R-O, Ag/Fe_3O_4/rGO(F)-AA-R-F are shown in Fig. 10a–d respectively. As shown in Fig. 10e, the plots of Ln (At/A0) at 400 nm are compared for as-prepared nanocomposites, in which Ag^+ ions have been reduced to Ag^0 element using ascorbic acid as reducing agent. The difference in the drying method of the catalyst affects the increase of the reaction rate. Drying the catalyst in a freeze dryer has a greater effect on increasing the reaction rate than the method of drying in the oven due to the creation of more porosity. In addition, as can be seen in the plot, the catalyst that uses freeze dried-graphene oxide as a substrate (Ag/Fe_3O_4/rGO(F)-AA-U-O, Ag/Fe_3O_4/rGO(F)-AA-U-F) compared to (Ag/Fe_3O_4/rGO(O)-AA-U-O, Ag/Fe_3O_4/rGO(O)-AA-U-F) was more effective than the other catalyst. To investigate the performance of Fe_3O_4/GO, which serves as a precursor for the preparation of Ag magnetic composites, sodium borohydride was used in the test for the reduction of 4-NP. The results showed that this material exhibited no impact on the catalytic reduction of 4-NP over a duration of 50 min (Fig. S3).

In this experiment, CTAB, a cationic surfactant, was used as a stabilizer in order to homogenize the distribution of Ag nanoparticles on the reduced graphene oxide substrate. The positively charged head groups of CTAB adsorb onto the surface of the Ag NPs, creating a protective layer that prevents aggregation through electrostatic repulsion. Additionally, the long hydrophobic tails of CTAB extend into the solution, creating a steric barrier that further prevents nanoparticle aggregation. The use of CTAB is crucial for increasing the catalytic activity of the nanocomposites. By preventing the aggregation of Ag NPs, CTAB ensures a larger surface area and a higher number of active sites available for catalytic reactions. This leads to improved reaction kinetics and higher catalytic activity, as evidenced by the enhanced performance of the CTAB-stabilized nanocomposites in the reduction of 4-NP[34,35]. It was expected that the performance of the catalyst would improve with a better distribution of the particles on the graphene oxide substrate. The UV spectrum of the catalytic reduction of 4-NP in the presence of excess $NaBH_4$ by Ag/rGO(O)-HH-R-O-CTAB, Ag/rGO(O)-HH-R-F-CTAB, nanocomposite catalysts are shown in Fig. 11a, b respectively. As shown in Fig. 11c, the catalyst prepared with hydrazine hydrate as a reducing agent and CTAB demonstrated improved performance in both powdered and aerogel forms compared to the same catalyst synthesized without CTAB (Table 2.entries 4, 14, 15). However, when cellulose nanofibers and ascorbic acid were used as reducing agents along with the stabilizer CTAB, no enhancement in catalytic performance was observed (Fig. S4).

The performance of the Ag nanocomposite catalysts synthesized in this research on the catalytic reduction of 4-NP including the reaction time, rate, and activity parameter (k´ = k/m) is shown in Table 2, k refers to rate constant and m refers to mass of catalyst.

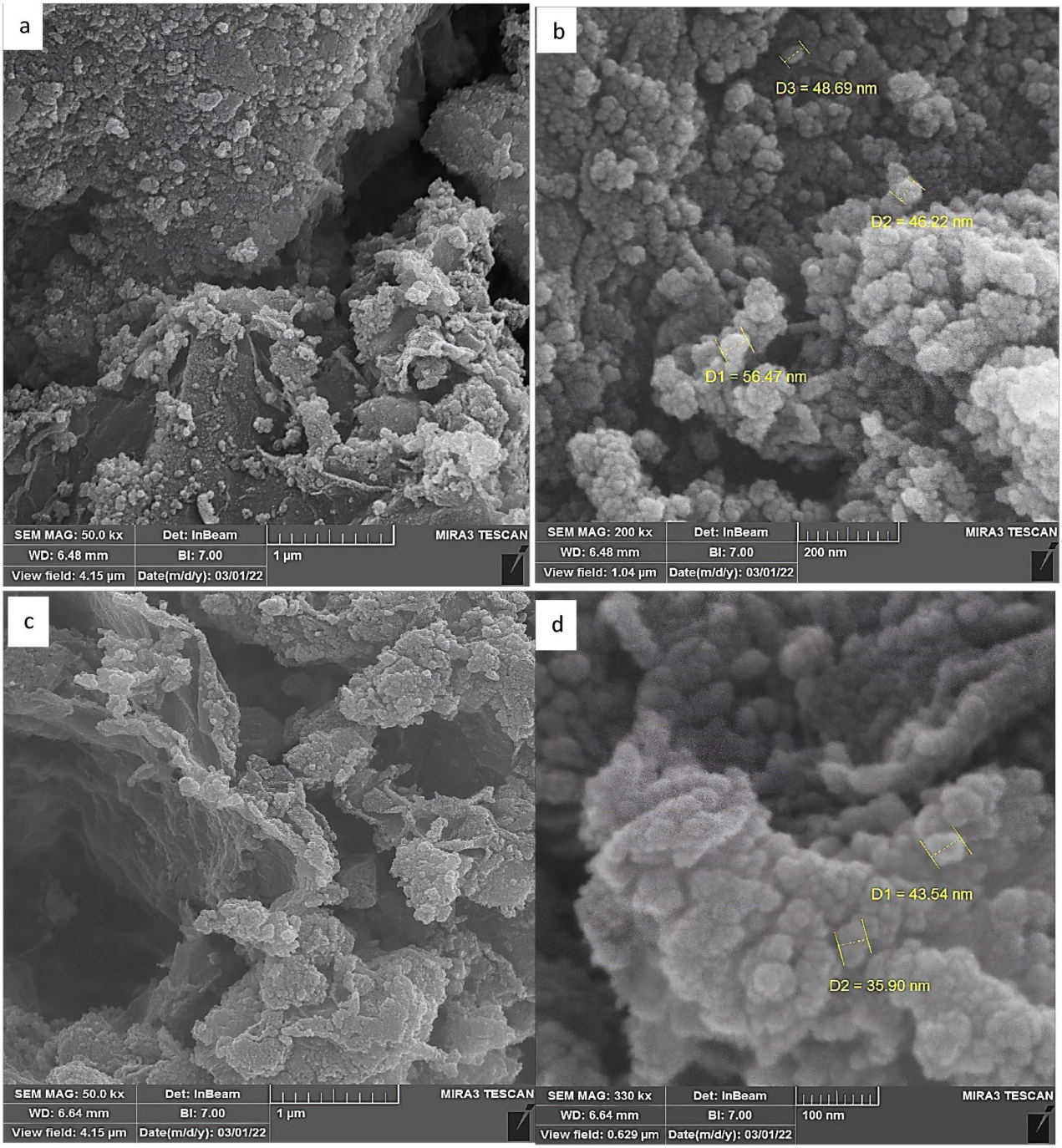

Fig. 4. FESEM micrographs of (**a**, **b**) Ag/Fe_3O_4/rGO(O)-AA-U-O, (**c**, **d**) Ag/Fe_3O_4/rGO(O)-AA-U-F. (**e**-**j**) EDS mapping and elemental analysis of Ag/Fe_3O_4/rGO(O)-AA-U-F.

Effect of reaction temperature on 4-NP reduction

In order to evaluate the effectiveness of the Ag/rGO(O)-AA-R-F catalyst for 4-NP reduction, it is important to take into account the environmental conditions and conduct temperature-dependent studies. The dependence of the reaction rate on temperature is illustrated in Fig. 12a, which plots the change in $\ln(A_t/A_0)$ as a function of time at different temperatures. As the temperature increased, the reduction rates exhibited a linear increase. Investigating the temperature-dependent kinetics of 4-NP reduction reaction facilitates the determination of key thermodynamic parameters, including entropy, and enthalpy.The activation enthalpy ($\Delta H^{\neq}$) and entropy ($\Delta S^{\neq}$) were calculated using the Eyring Eq. (3)[36] by plotting $\ln(k_{obs}/T)$ vs. 1/1000 T as illustrated in Fig. 12b and the calculated values were found to be $\Delta H^{\neq} = 17.19\ kJ.mol^{-1}$ and $\Delta S^{\neq} = -192.2 J.mol^{-1}.K^{-1}$. In this equation k_b is the Boltzmann constant (1.381×10^{-23} J.K^{-1}), h is the Planck constant (6.626×10^{-34} J.s) and R is the universal gas constant (8.314 J. K^{-1}. mol^{-1}).

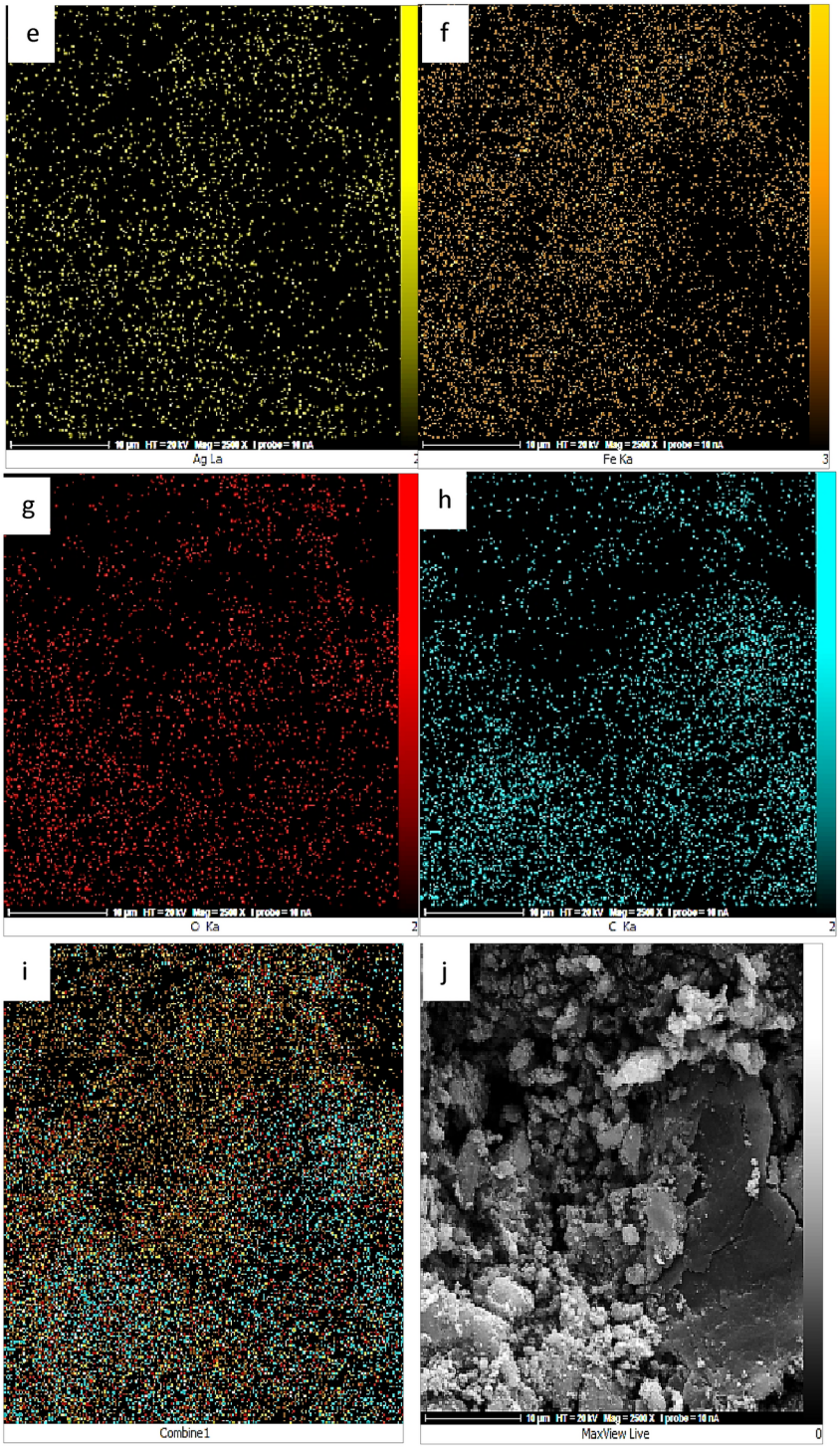

Elt	W%	A%
C	34.61	53.59
O	31.35	36.44
Fe	25.55	8.51
Ag	8.50	1.46

Figure 4. (continued)

$$Ln\left(\frac{k_{obs}}{T}\right) = Ln\left(\frac{k_b}{h}\right) + \left(\frac{\Delta S^{\neq}}{R}\right) - \left(\frac{\Delta H^{\neq}}{R}\right)\left(\frac{1}{T}\right) \quad (3)$$

$$\Delta S^{\neq} = -192.2 J.mol^{-1}.K^{-1}$$

$$\Delta H^{\neq} = 17.19 kJ.mol^{-1}$$

The apparent activation energy (Ea) can be determined using the Arrhenius Eq. (4)[37], where k_{obs} represents the apparent rate constant, T represents the temperature, R is the molar gas constant, and A is the pre-exponential

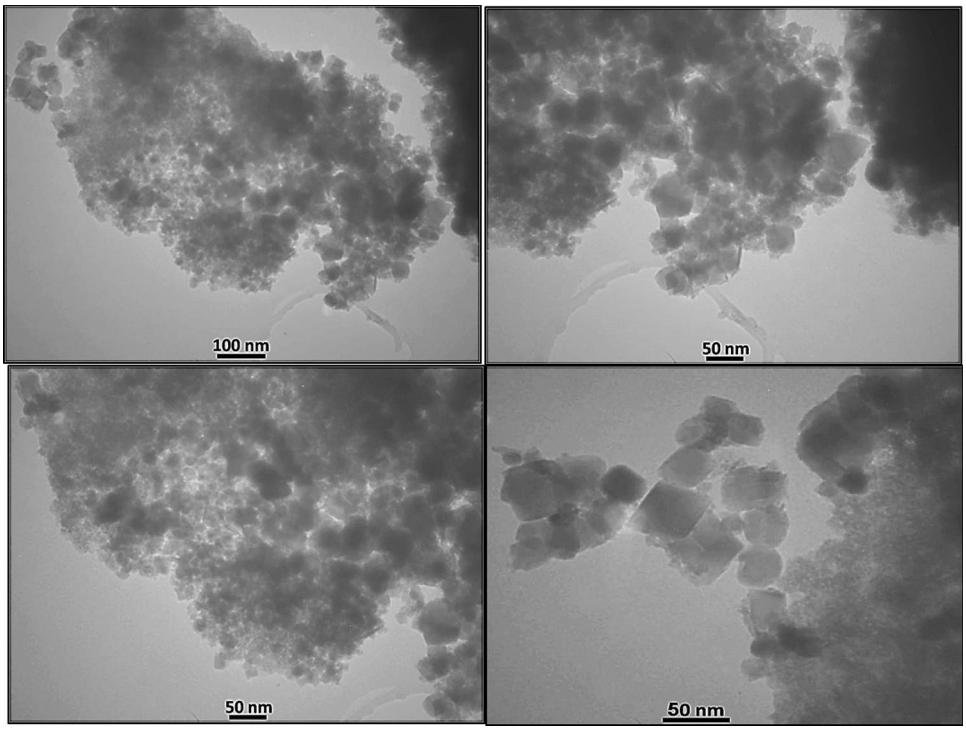

Fig. 5. TEM images Ag/Fe_3O_4/rGO(O)-AA-U-F.

	S_{BET} ($m^2.g^{-1}$)	Pore volume ($cm^3.g^{-1}$)	Mean pore diameter (nm)
Ag/rGO(O)-AA-R-O	18.41	0.086	18.44
Ag/rGO(O)-AA-R-F	39.91	0.056	5.63
Ag/Fe_3O_4/rGO(O)-AA-U-F	226.9	0.43	7.74

Table 1. BET surface areas, pore volume and pore diameter of different composites.

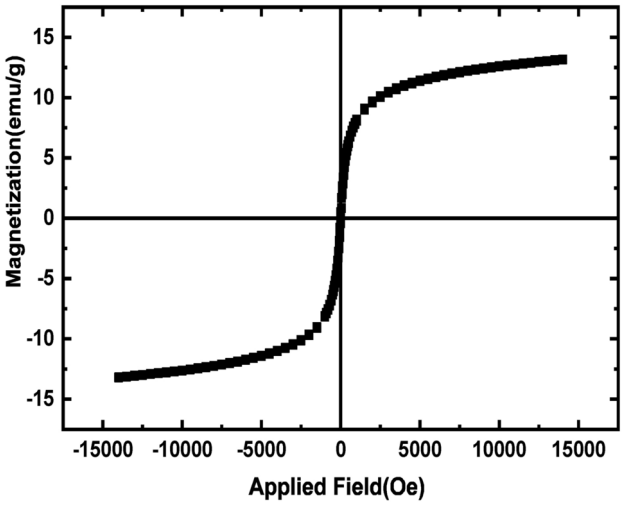

Fig. 6. Magnetization curve of Ag/Fe_3O_4/rGO(O)-AA-U-O.

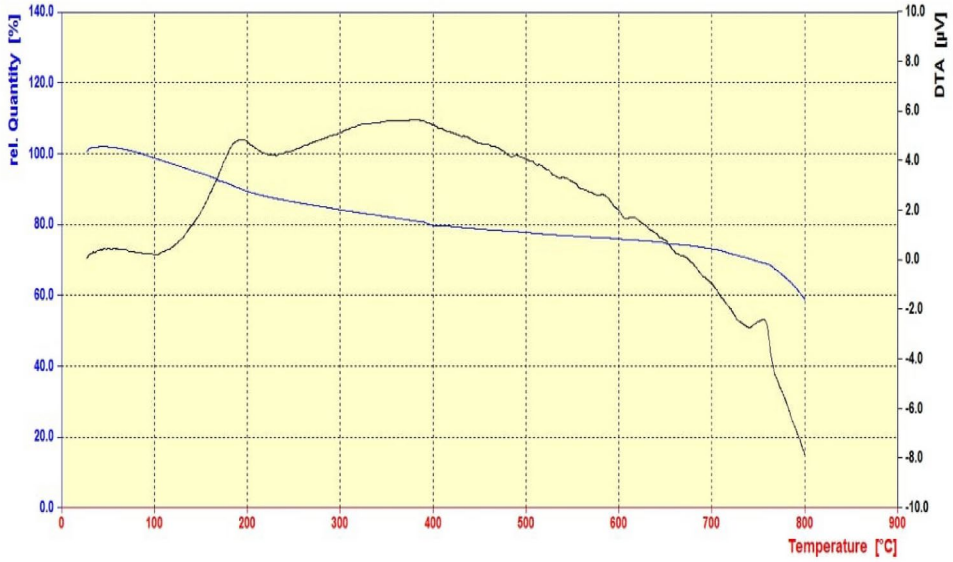

Fig. 7. TGA and DTA curves for Ag/Fe_3O_4/rGO(O)-AA-U-O.

factor(Arrhenius factor). Figure 12c illustrates the linear fitting of ln k_{obs} against 1000/T. The calculated value of the apparent activation energy was found to be 19.73 $kJ.mol^{-1}$

$$Ln\left(k_{obs}\right) = Ln\left(A\right) - \left(\frac{E_a}{R}\right)\left(\frac{1}{T}\right) \tag{4}$$

$$E_a = 19.73 kJ.mol^{-1}$$

The reduction of 4-NP using the Ag/rGO(O)-AA-R-F catalyst shows a strong temperature dependence, with the reaction rate increasing linearly. The low activation energy (E_a), indicating efficient catalysis. Thermodynamic parameters (enthalpy and enthropy) suggest a more ordered transition state. These findings confirm the catalyst's effectiveness in accelerating the reaction under mild conditions.

To compare catalytic activity with the reported catalysts used for 4-NP reduction, the catalytic activity was summarized in Table 3. The catalytic activity of Ag/Fe_3O_4/rGO(O)-AA-U-F was acceptable compare to the other listed catalysts in Table 3.

Conclusions

This study successfully synthesized and characterized Ag/rGO and Ag/Fe_3O_4/rGO nanocomposites using various reducing agents (ascorbic acid, hydrazine hydrate, sodium borohydride, and cellulose nanofibers) and synthesis methods (reflux, hydrothermal, and ultrasonic irradiation). Among the synthesized nanocomposites, Ag/Fe_2O_4/rGO(O)-AA-U-F demonstrated the highest catalytic activity for the reduction of 4-NP, achieving a pseudo-first-order rate constant (k) of 1.81 min^{-1} and a specific activity parameter (k') of 180.77 $min^{-1}.g^{-1}$. This exceptional performance is attributed to its high specific surface area (226.9 m^2/g), mesoporous structure, and uniform distribution of Ag and Fe_2O_4 nanoparticles on the rGO surface. The use of ascorbic acid (AA) as a reducing agent, combined with freeze-drying (F), significantly enhanced catalytic performance. Structural and morphological analyses, including XRD, FT-IR, FE-SEM, and TEM, confirmed the successful formation of Ag and Fe_2O_4 nanoparticles on the rGO substrate. Temperature-dependent kinetic studies revealed a low activation energy (E_a = 19.73 kJ/mol), indicating efficient catalytic activity under mild conditions. The results revealed that nanocomposites synthesized with ascorbic acid exhibited the highest catalytic activity, while the use of stronger reducing agents, such as sodium borohydride, led to a reduction in catalytic performance. These findings underscore the importance of selecting suitable reducing agents and synthesis methods in designing efficient catalysts for environmental and industrial applications.

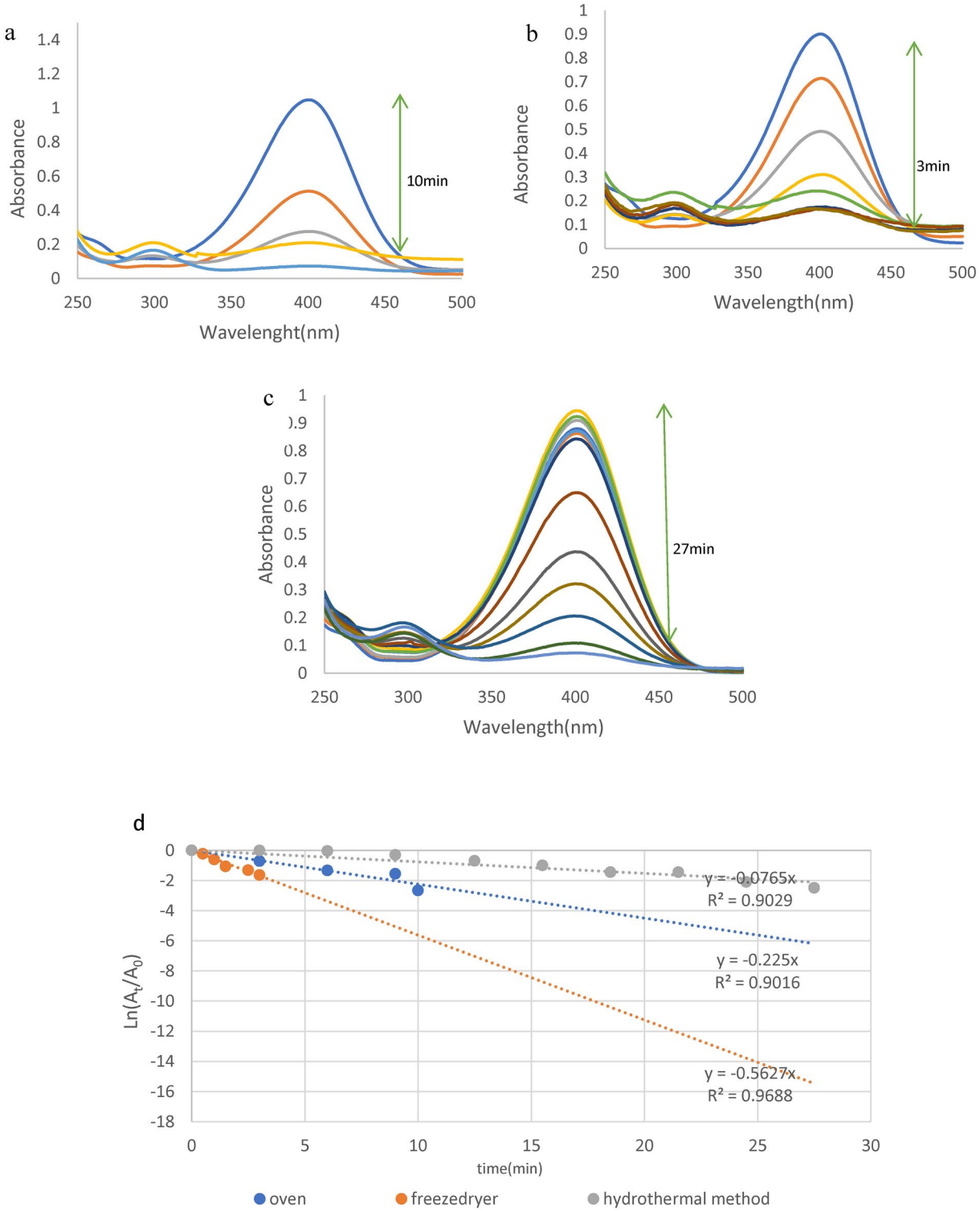

Fig. 8. UV–Vis spectra of 4-NP reduction using (**a**) Ag/rGO(O)-AA-R-O (**b**) Ag/rGO(O)-AA-R-F (**c**) Ag/rGO(O)-AA-H-O (**d**) The plot of Ln (A_t/A_0) versus time using ascorbic acid reductant.

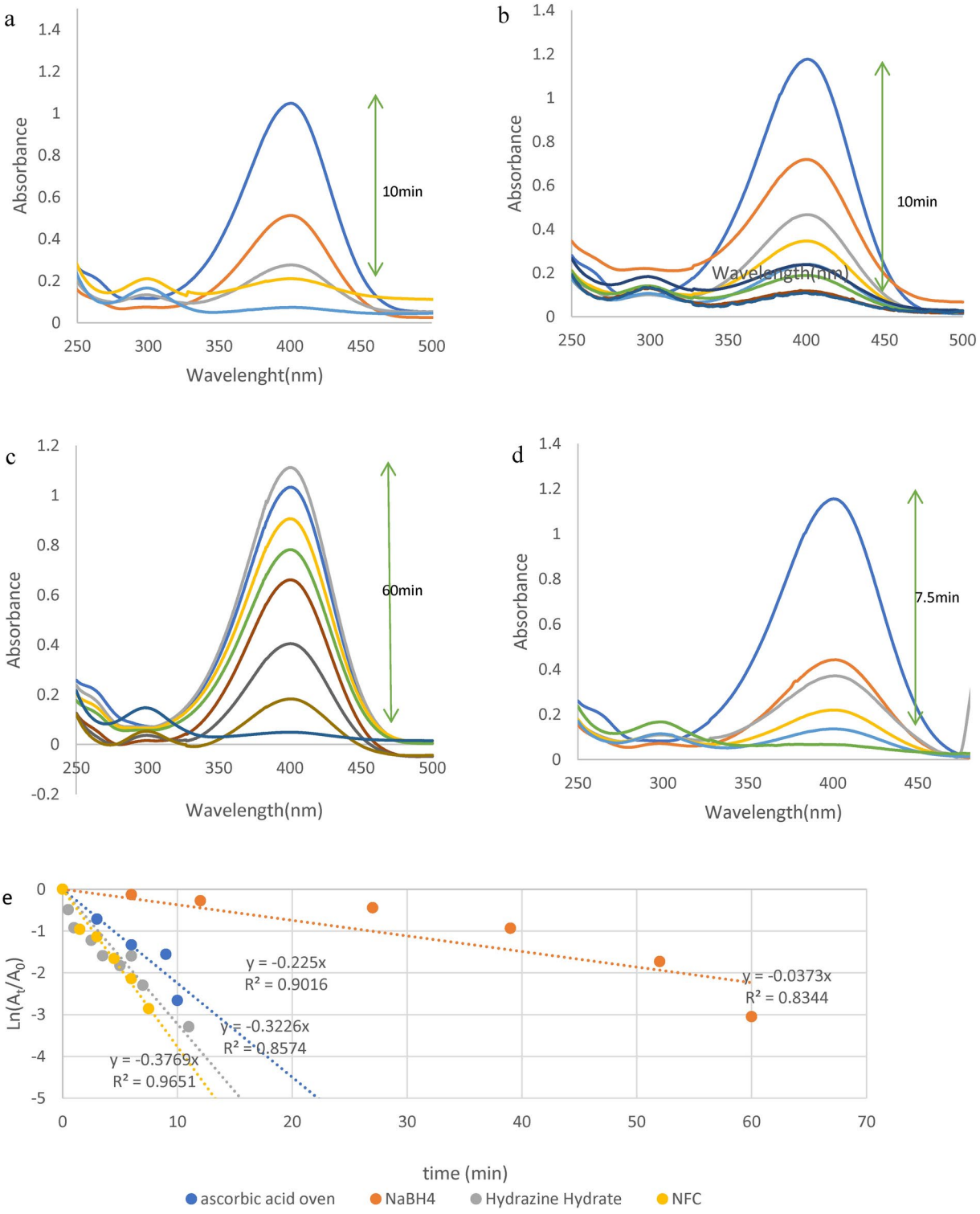

Fig. 9. UV–Vis spectra of 4-NP reduction using (**a**) Ag/rGO(O)-AA-R-O (**b**) Ag/rGO(O)-HH-R-O (**c**) Ag/rGO(O)-SBH-R-O (**d**) Ag/rGO(O)-NFC-R-O (**e**) The effect of various reducers on the rate constant diagrams.

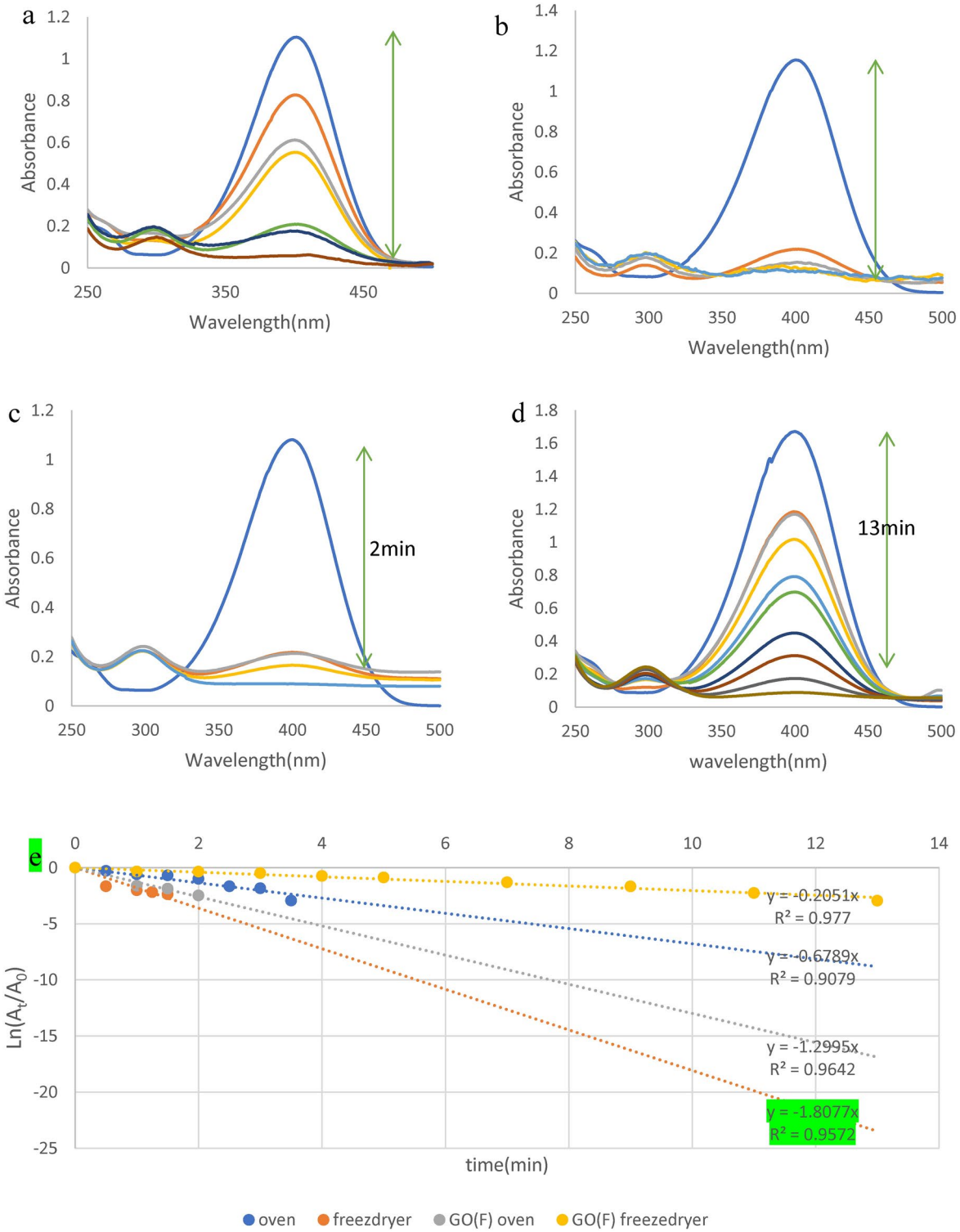

Fig. 10. UV–Vis spectra of 4-NP reduction using (**a**) Ag/Fe_3O_4/rGO(O)-AA-U-O (**b**) Ag/Fe_3O_4/rGO(O)-AA-U-F (**c**) Ag/Fe_3O_4/rGO(F)-AA-U-O (**d**) Ag /Fe_3O_4/rGO(F)-AA-U-F (**e**) Rate constant plot for silver magnetic catalysts using ascorbic acid reductant.

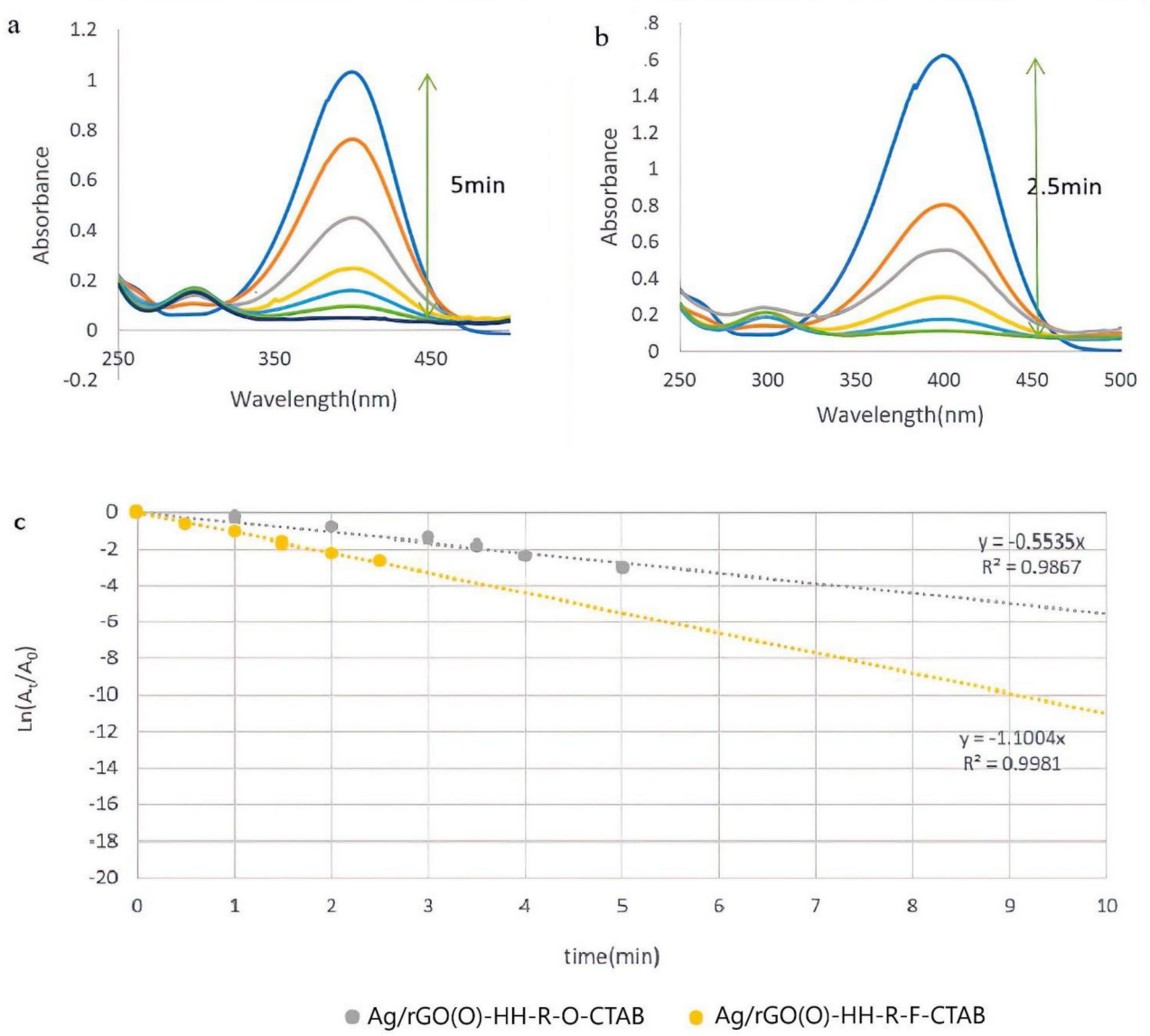

Fig. 11. UV–Vis spectra of 4-NP reduction using (**a**) Ag/rGO(O)-HH-R-O-CTAB (**b**) Ag/rGO(O)-HH-R-F-CTAB and (**c**) Rate constant plots for silver catalysts with CTAB.

	Catalyst	4-NP reduction		
		Time (min)	Rate	k´ ($min^{-1}. g^{-1}$)
1	Ag/rGO(O)-AA-R-O	10	y = − 0.225x R^2 = 0.9016	22.5
2	Ag/rGO(O)-AA-R-F	3	y = − 0.5627x R^2 = 0.9688	56.27
3	Ag/rGO(O)-AA-H-O	27	y = − 0.0765x R^2 = 0.9029	7.65
4	Ag/rGO(O)-HH-R-O	11	y = − 0.2986x R^2 = 0.8097	29.86
5	Ag/rGO(O)-SBH-R-O	60	y = − 0.0373x R^2 = 0.8344	3.73
6	Ag/rGO(O)-NFC-R-O	7.5	y = − 0.3769x R^2 = 0.9651	37.69
7	Ag/rGO(O)-NFC-R-F	4	y = − 0.6682x R^2 = 0.9931	66.82
8	Ag/Fe3O4/rGO(O)-NFC-U–O	8	y = − 0.4055x R^2 = 0.9594	40.55
9	Ag/Fe3O4/rGO(O)-NFC-U-F	7	y = − 0.5272x R^2 = 0.9434	52.72
10	Ag/Fe3O4/rGO(O)-AA-U–O	3.5	y = − 0.6789x R^2 = 0.9079	67.89
11	Ag/Fe3O4/rGO(O)-AA-U-F	1.5	y = − 1.8077x R^2 = 0.9572	180.77
12	Ag/Fe3O4/rGO(F)-AA-U–O	2	y = − 1.2995x R^2 = 0.9642	129.95
13	Ag/Fe3O4/rGO(F)-AA- U-F	13	y = − 0.2051x R^2 = 0.977	20.51
14	Ag/rGO(O)-HH-R-O-CTAB	5	y = − 0.5535x R^2 = 0.9615	55.35
15	Ag/rGO(O)-HH- R- F-CTAB	2.5	y = − 1.1004x R^2 = 0.9936	110.0

Table 2. The performance of the Ag nanocomposite catalysts in reduction of 4-NP.

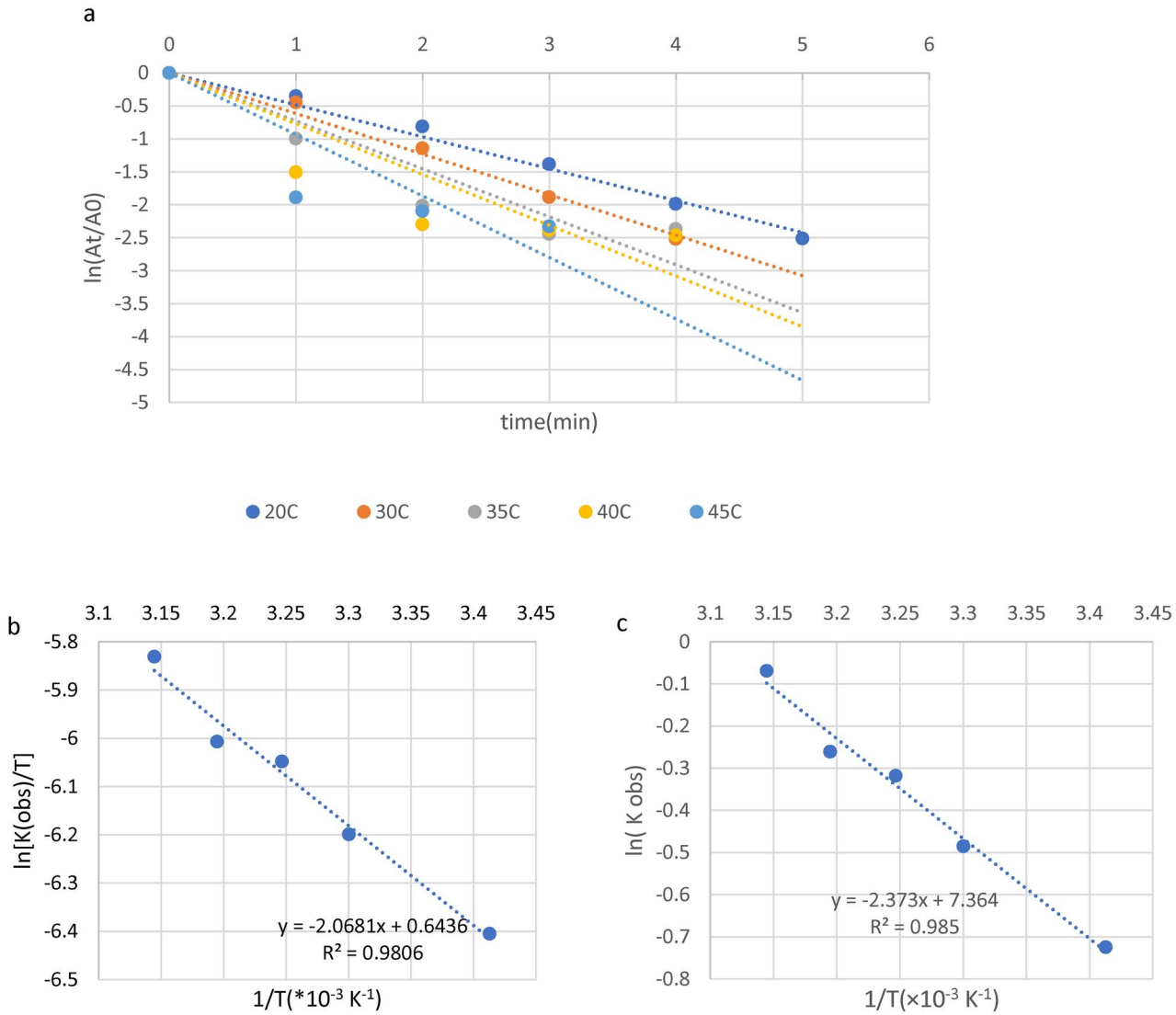

Fig. 12. (**a**) Rate constant plot of Ag/rGO(O)-AA-R-F catalyst at different temperatures, (**b**) The plot of Ln (k_{obs}/T) versus 1000/T, (**c**) The plot of Ln (k_{obs}) versus 1000/T.

Entry	Catalyst	Catalyst dosage (mg)	Concentration of pollutant (mM)	Time(min)	k(min^{-1})	k´ (min^{-1}. g^{-1})	Refs.
1	Ag/CTAB/NCC	42	20	…	0.324	7.71	[35]
2	Fe_3O_4/NFC/Ag-1	10	0.4	1.5	2.44	244.2	[27]
3	Ag/NCC	30	20	3	0.498	16.6	[26]
4	Ag/Fe_3O_4/GO	10	0.2	12	0.304	30.4	[1]
5	rGO/Ag NPs	0.5	0.072	3	1.26	2520	[38]
6	Fe_3O_4/Ag/NG	0.5	0.1	2.5	1.08	2160	[39]
7	rGO/CNT/Fe/Ag	0.2	0.12	6	0.88	113,058.6	[40]
8	AgNPs/RGO			6	0.38		[41]
9	rGO/Fe_3O_4/Ag NH	0.35	1	10	0.37	1057.14	[42]
10	rGO–Ag nanocomposite	5×10–5	1	17	0.34	680	[43]
11	Ag/Fe_3O_4/rGO(O)-AA-U-F	10	20	1.5	1.81	180.77	This work

Table 3. Comparison of catalytic activity for the reduction of 4-NP with different catalysts.

Data availability

All data generated or analyzed during this study are included in this manuscript and supplementary information.

Received: 18 January 2025; Accepted: 14 April 2025
Published online: 25 April 2025

References

1. Doan, V. D., Nguyen, N. V., Nguyen, T. L. H., Tran, V. A. & Le, V. T. High-efficient reduction of methylene blue and 4-NP by silver nanoparticles embedded in magnetic graphene oxide. *Environ. Sci. Pollut. Res.* **30**, 71543–71553 (2023).
2. Mejía, Y. R. & Reddy Bogireddy, N. K. Reduction of 4-NP using green-fabricated metal nanoparticles. *RSC Adv.* **12**, 18661–18675 (2022).
3. Pierre, A. C. & Pajonk, G. M. Chemistry of aerogels and their applications. *Chem. Rev.* **102**, 4243–4266 (2002).
4. Yu, W., Sisi, L., Haiyan, Y. & Jie, L. Progress in the functional modification of graphene/graphene oxide: A review. *RSC Adv.* **10**, 15328–15345 (2020).
5. Barrios, E. et al. Nanomaterials in advanced, high-performance aerogel composites: A review. *Polymers (Basel).* **11**, 1–41 (2019).
6. Sinha, M. K. & Purcell, W. Reducing agents in the leaching of manganese ores: A comprehensive review. *Hydrometallurgy* **187**, 168–186 (2019).
7. Zhang, X. et al. Synthesis of graphene aerogels using cyclohexane and: N -butanol as soft templates. *RSC Adv.* **10**, 14283–14290 (2020).
8. Candelaria, S. L. et al. Nanostructured carbon for energy storage and conversion. *Nano Energy* **1**, 195–220 (2012).
9. Kgatle, M., Sikhwivhilu, K., Ndlovu, G. & Moloto, N. Degradation kinetics of methyl orange dye in water using trimetallic Fe/Cu/Ag nanoparticles. *Catalysts* **11**, 428 (2021).
10. Chen, T. et al. Facile preparation of Fe_3O_4/Ag/RGO reusable ternary nanocomposite and its versatile application as catalyst and antibacterial agent. *J. Alloys Compd.* **876**, 160153 (2021).
11. Parthiban, D., Ramasamy, M., Chinnaswamy, K. & Ayyanan, V. Mangrove tree aerial root extract mediated green synthesis of Ag/Fe_3O_4/rGO nanocomposite and its application as a catalyst. *Environ. Sci. Pollut. Res.* **31**, 59490–59506 (2024).
12. Liu, Y. et al. Metal or metal-containing nanoparticle@MOF nanocomposites as a promising type of photocatalyst. *Coord. Chem. Rev.* **388**, 63–78 (2019).
13. Heidari, H. Ag nanoparticle/nanofibrillated cellulose composite as an effective and green catalyst for reduction of 4-NP. *J. Clust. Sci.* **29**, 475–481 (2018).
14. Guimarães, A. C. P. et al. Dry reforming of methane over Ni catalysts supported on hierarchical ZSM-5 and USY zeolites. *Catal. Today* **447**, 115159 (2025).
15. Eslaminejad, S., Rahimi, R. & Fayazi, M. Green decoration of Pd nanoparticles on MXene/metal organic framework support for photocatalytic degradation of ofloxacin. *J. Ind. Eng. Chem.* **141**, 94–103 (2024).
16. Dayana, B. M. et al. Solution-gelation synthesis of silver nanoparticles utilizing Justicia tranquebariensis extract for antibacterial, antioxidant, antifungal and anticancer activity. *J. Sol-Gel Sci. Technol.* **110**, 828–841 (2024).
17. Alam, F., Ansari, S. A., Khan, W., Khan, M. E. & Naqvi, A. H. Synthesis, structural, optical and electrical properties of IN-SITU synthesized polyaniline/silver nanocomposites. *Funct. Mater. Lett.* **5**, 1–5 (2012).
18. Ansari, S. A., Khan, M. M., Ansari, M. O. & Cho, M. H. Silver nanoparticles and defect-induced visible light photocatalytic and photoelectrochemical performance of Ag@m-TiO_2 nanocomposite. *Sol. Energy Mater. Sol. Cells* **141**, 162–170 (2015).
19. Khan, M. M. et al. Electrochemically active biofilm assisted synthesis of Ag@CeO_2 nanocomposites for antimicrobial activity, photocatalysis and photoelectrodes. *J. Colloid Interface Sci.* **431**, 255–263 (2014).
20. Devi, N. M., BaQais, A., Debnath, A. K., Alam, M. W. & Singh, N. K. Improved photodetection capabilities of Ag@CeO_2 Nanorod composite array using GLAD technique. *Ceram. Int.* **48**, 30107–30117 (2022).
21. Pratapkumar, C. et al. Structural, photocatalytic and electrochemical studies on facile combustion synthesized low-cost nano chromium (III) doped polycrystalline magnesium aluminate spinels. *J. Sci. Adv. Mater. Devices* **6**, 462–471 (2021).
22. Alam, M. W. et al. Enhanced photocatalytic performance of Ag_3PO_4/Mn-ZnO nanocomposite for the degradation of tetracycline hydrochloride. *Crystals* **12**, 1156 (2022).
23. Philip, D. Green synthesis of gold and silver nanoparticles using Hibiscus rosa sinensis. *Physica E* **42**, 1417–1424 (2010).
24. Sun, Y. & Xia, Y. Shape-controlled synthesis of gold and silver nanoparticles. *Science* **298**, 2176–2179 (2002).
25. Turkevich, J., Stevenson, P. C. & Hillier, J. A study of the nucleation and growth processes in the synthesis of colloidal gold. *Discuss. Faraday Soc.* **11**, 55. https://doi.org/10.1039/df9511100055 (1951).
26. Heidari, H. & Karbalaee, M. Ultrasonic assisted synthesis of nanocrystalline cellulose as support and reducing agent for Ag nanoparticles: Green synthesis and novel effective nanocatalyst for degradation of organic dyes. *Appl. Organometall. Chem.* **33**, e5070 (2019).
27. Heidari, H. & Aliramezani, F. Reductant-free and in-situ green synthesis of Ag nanoparticles on Fe_3O_4@Nanocellulose and their catalytic activity for the reduction of dyes. *ChemistrySelect* **6**, 1223–1229 (2021).
28. Marcano, D. C. et al. Improved synthesis of graphene oxide. *ACS Nano* **4**, 4806–4814 (2010).
29. Su, J., He, S., Zhao, Z., Liu, X. & Li, H. Efficient preparation of cetyltrimethylammonium bromide-graphene oxide composite and its adsorption of Congo red from aqueous solutions. *Colloids Surfaces A Physicochem. Eng. Asp.* **554**, 227–236 (2018).
30. Zhu, Y. et al. Graphene and graphene oxide: Synthesis, properties, and applications. *Adv. Mater.* **22**, 3906–3924 (2010).
31. Abbasi, L., Hedayati, K. & Ghanbari, D. Magnetic properties and kinetic roughening study of prepared polyaniline: Lead ferrite, cobalt ferrite and nickel ferrite nanocomposites electrodeposited thin films. *J. Mater. Sci. Mater. Electron.* **32**, 14477–14493 (2021).
32. Abdel-Aal, S. K. & Abdel-Rahman, A. S. Graphene influence on the structure, magnetic, and optical properties of rare-earth perovskite. *J. Nanopart. Res.* **22**, 267 (2020).
33. Vyazovkin, S. et al. Thermal analysis. *Anal. Chem.* **83**, 4936–4949 (2011).
34. Sui, Z. M. et al. Capping effect of CTAB on positively charged Ag nanoparticles. *Phys. E* **33**, 308–314 (2006).
35. Heidari, H. & Karbalaee, M. Silver-nanoparticle supported on nanocrystalline cellulose using cetyltrimethylammonium bromide: Synthesis and catalytic performance for decolorization of dyes. *J. Nanostruct.* **11**, 48–56 (2021).
36. Kumar, A., Belwal, M., Maurya, R. R., Mohan, V. & Vishwanathan, V. Heterogeneous catalytic reduction of anthropogenic pollutant, 4-nitrophenol by Au/AC nanocatalysts. *Mater. Sci. Energy Technol.* **2**, 526–531 (2019).
37. Lourens, A., Falch, A. & Malgas-Enus, R. Nano-Ni/Cu decorated iron oxide for catalytic reduction of 4-nitrophenol. *Mater. Chem. Phys.* **315**, 129022 (2024).
38. Sun, W. et al. Biogenic synthesis of reduced graphene oxide decorated with silver nanoparticles (rGO/Ag NPs) using table olive (Olea europaea) for efficient and rapid catalytic reduction of organic pollutants. *Chemosphere* **310**, 136759 (2023).
39. Dai, Y. M., Chen, Y. S., Zhu, W. X., Lin, Z. W. & Tsai, M. H. In-situ fabrication of Ag nanoparticles decorated magnetic N-doped graphene heterogeneous catalyst for the catalytic reduction of 4-NP. *J. Taiwan Inst. Chem. Eng.* **163**, 105524 (2024).
40. Tran, X. T., Hussain, M. & Kim, H. T. Facile and fast synthesis of a reduced graphene oxide/carbon nanotube/iron/silver hybrid and its enhanced performance in catalytic reduction of 4-nitrophenol. *Solid State Sci.* **100**, 106107 (2020).

41. Hazra Chowdhury, A., Hazra Chowdhury, I. & Islam, S. M. One-pot green synthesis of AgNPs@RGO for removal of water pollutant and chemical fixation of CO_2 under mild reaction conditions. *J. Inorg. Organomet. Polym. Mater.* **30**, 5270–5282 (2020).
42. Thu, T. V. et al. Green synthesis of reduced graphene oxide/Fe_3O_4/Ag ternary nanohybrid and its application as magnetically recoverable catalyst in the reduction of 4-NP. *Appl. Organomet. Chem.* **31**, 1–9 (2017).
43. Belachew, N., Meshesha, D. S. & Basavaiah, K. Green syntheses of silver nanoparticle decorated reduced graphene oxide using l-methionine as a reducing and stabilizing agent for enhanced catalytic hydrogenation of 4-NP and antibacterial activity. *RSC Adv.* **9**, 39264–39271 (2019).

Acknowledgements

The authors gratefully acknowledge from the Research Council of Alzahra University for financial support.

Author contributions

B.K. and H.H. contributed to the design and implementation of the research. B.K. Conceptualization, Validation, Writing—original draft, H.H. Conceptualization, Validation, Writing—original draft, Writing—review & editing, Project administration.

Competing interests

The authors declare no competing interests.

Additional information

Supplementary Information The online version contains supplementary material available at https://doi.org/10.1038/s41598-025-98540-9.

Correspondence and requests for materials should be addressed to H.H.

Reprints and permissions information is available at www.nature.com/reprints.

Publisher's note Springer Nature remains neutral with regard to jurisdictional claims in published maps and institutional affiliations.